Transport in Porous Media (2023) 150:307–326
https://doi.org/10.1007/s11242-023-02010-7

Flow Field Characterisation of Gaseous Flow in a Packed Bed by Particle Image Velocimetry

C. Velten[1] · **K. Zähringer**[1]

Received: 8 May 2023 / Accepted: 12 August 2023 / Published online: 26 August 2023

Abstract

Packed beds with gaseous flow are used in many industrial processes with high energy and resource consumption. This study provides velocity data of the gas flow through a model packed bed of 40 mm spheres arranged in body centred cubic packing obtained by Particle Image Velocimetry to allow for validation of numerical calculations which are often used for process optimization. Results are presented exemplarily for a particle Reynolds number range from 200 to 500. The flow fields are discussed in terms of inlet conditions to the empty reactor, symmetry and height independent flow structure above the bed and measurements in the optically accessible interstices of the bed. The measurement of a sufficient number of snap-shots for each measurement condition and location allowed also for the determination of the turbulent kinetic energy. Above the bed, low frequency oscillations of the flow are observed, that increase with the Reynolds number. In the interior of the bed, fluctuations are much less pronounced. The appearing flow structures are not significantly influenced by different particle Reynolds numbers, but the velocity magnitude changes.

Article Highlights

- **Particle image velocimetry in particle assemblies with gas flow for particle Reynolds numbers 200–500.**
- **Inlet conditions, symmetry, bed height independent flow structures and turbulence data above and inside the packed bed.**
- **Database provided for the validation of numerical calculations.**

Keywords Gaseous flow in packed bed · Body centred cubic packing of spherical particles · Particle image velocimetry (PIV) · Free surface and interstitial flow · Open data base

✉ C. Velten
christin.velten@ovgu.de

[1] Lehrstuhl für Strömungsmechanik und Strömungstechnik, Otto-von-Guericke-Universität Magdeburg, 39106 Magdeburg, Germany

1 Introduction

Many industrial processes such as drying processes, catalytic reactions or calcination are based on a packed bed reactor with gaseous flow. Most of these applications come with a high energy and resource consumption, which can be decreased by an optimized process operation in terms of heat and mass transfer. Both are influenced by the flow characteristics of the gas passing through the reactor. A common tool for such process optimizations are numerical calculations, since industrial reactors are seldom accessible for measurement techniques. Nevertheless, these simulation tools have to be validated by experimental findings and use models, obtained from detailed measurements in idealized model reactors.

For a better understanding of the gas flow in such model packed beds, different velocimetry techniques, preferably non-intrusive methods, which do not disturb the flow, can be applied. This includes for example tomographic techniques such as Magnetic Resonance Imaging (MRI) (e.g. Sederman et al. (1997), Suekane et al. (2003), Lovreglio et al. (2018)), or optical measurements like Laser Doppler Anemometry (LDA) (Giese et al. 1998), Particle Tracking Velocimetry (PTV) (e.g. Moroni and Cushman (2001), Hassan and Dominguez-Ontiveros (2008)), Particle Image Velocimetry (PIV), (e.g. Pokrajac and Manes (2009), Khayamyan et al. (2017b), Khayamyan et al. (2017a)), or tomographic PIV (Larsson et al. 2018). Each technique comes with its specific advantages and drawbacks.

While MRI flow measurements are mostly carried out in liquids due to strong challenges in the needed polarization of gases and the low resolution in space and time (Gladden et al. 2006; Poelma 2020), its clear advantage is that no optical access is needed. The use of transparent materials is mandatory for the use of the aforementioned optical techniques, introducing optical distortions due to differences in the refractive index of fluid and bed material. Typically, refractive index matching (RIM) (Wiederseiner et al. 2011) is applied, but obviously not available for gases. For *liquid*–solid systems the liquid can be chosen to match the refractive index of the packing material (e.g. Hassan and Dominguez-Ontiveros (2008)) or vice versa (e.g. Harshani et al. (2017)). Therefore, pore scale based velocity measurements are limited to transparent *liquid*–solid systems. The application of similarity theory, by the analysis of dimensionless numbers such as the particle Reynolds number, could draw analogies between the gas and the liquid system. To the best of the authors knowledge, no such work, showing and proofing this analogy assumption in packed beds is published up to now, also caused by the lack of data for gaseous flows.

Almost no velocity data inside gas–solid packed beds is available. Measurements with hot wire anemometry (Morales et al. 1951; Schwartz and Smith 1953), representing an intrusive method, allow to investigate the gas flow in different packing arrangements, the influence of different particle geometries and sizes as well as different Reynolds numbers. (Shaffer et al. 2013) report on optical velocity measurements without RIM in the near wall zone of fluidized beds, differing strongly in terms of the mechanism and particle size from the vertical fixed bed application considered here. First approaches to overcome the lack of data have been presented by our group for transparent systems with different approaches. Kováts et al. (2015) worked with gas flows through an assembly of hollow spheres and applied a special calibration procedure, relying on different calibration zones, to handle the optical distortions appearing in the absence of an index matched fluid. Martins et al. (2018a, b) applied a ray tracing based correction method to evaluate the flow field of a jet behind different sphere arrangements.

Since the evaluation of the flow through a vertical packed bed system by optical methods with RIM is closest to the application and data provided in this study, those literature results will be discussed more in detail in the following.

By applying RIM for the realisation of LDA measurements in randomly packed beds with differently shaped particles (spheres, deformed spheres, cylinders and Raschig rings), oscillations of the flow field were reported in dependency of the local porosity of the packed bed for measurements above and inside the packing (Giese et al. 1998). The particle Reynolds number range of the aforementioned study is similar to the present study (up to $Re_P = 500$) and reports that the averaged velocity profiles are constant along the packing when the flow is fully developed besides an inlet and outlet zone of approximately three particle length.

Since LDA delivers only point-wise data, PIV or PTV can be applied for a deeper understanding of the flow characteristics. Hassan et al. (Hassan and Dominguez-Ontiveros 2008) reported that vortices in the pores only appear for Re_P above 80 and their amount and size increases with the pore size. Vorticity increases in the pores close to the boundaries of the packing material. Starting from particle $Re_P = 300$, fully developed recirculation zones in the pore centre exist. For lower Re_P ($Re_P = 50$) the flow is not influenced by the vortices and goes straight upwards through the bed. For higher Re_P this main flow direction is kept, but with vortices formation in the pore centres.

For higher particle Reynolds numbers in the turbulent transition or fully turbulent range, Nguyen et al. (2019) reported that a strong bypass flow between the spheres and enclosure wall appears, leading to recirculation zones where the flow escapes from the bypassed region into free pore spaces. The existence of shear layers and recirculation zones between the spheres is verified by the analysis of Reynolds stress profiles as well as further characterization of 3D vertical flow structures by Taylor's hypothesis. The authors also stress, that an increase in Reynolds number does not lead to a significant increase in vortex formation.

For the lower particle Reynolds number range in randomly packed beds of glass spheres where the flow is not effected by inertia effects, different authors (e.g. Patil and Liburdy (2013), Wood et al. (2015)) reported that flow separation is absent and no recirculation zones appear. The flow structures remain the same when changing the particle Reynolds number. Following (Wood et al. 2015), maximum velocities inside the packing are determined to be approximately 3.7 times higher than the interstitial velocity.

For the validation of numerical models and simulations, the geometry of the packing as well as the inlet conditions have to be known exactly. For irregular packing the geometry can only be determined in RIM, thus *liquid*–solid, systems (Huang et al. 2008; Wood et al. 2015). For gaseous flows, a regular packing, like the body centred cubic packing (bcc) used in this study, avoids the difficulties arising from an unknown assembly for the setup of the numerical calculations. Additionally, regular packing's allow for measurements in the optically accessible interstices and not only in the freeboard above the packed bed. Some areas inside the regularly packed bed are accessible for illumination and camera views inside the bed, contrary to a random packing.

In this experimental study, an extensive data base is established for validation purposes in Computational Fluid Dynamics (CFD) and Discrete Element Method (DEM) calculations. Therefore, a complete as possible data set of gaseous flow velocities is acquired by the help of Particle Image Velocimetry (PIV) in the entrance zone, at the surface and in the interstices of a model body centred cubic packing reactor for a particle Reynolds number range from $200 \leqq Re_P \leqq 500$. Time series and mean velocity fields, as well as derived turbulence quantities are obtained. In this paper, we present the main

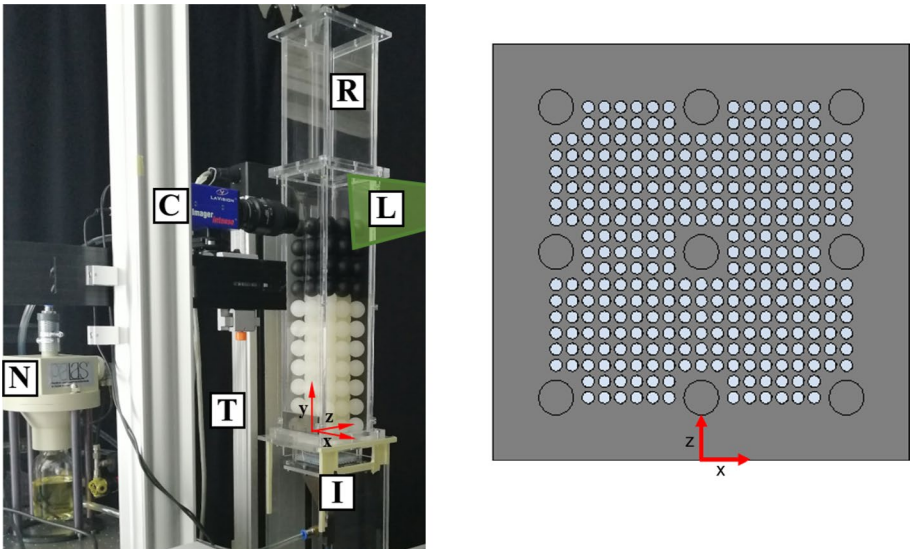

Fig. 1 Left: Experimental setup consisting of a bulk reactor (R), the air inlet (I), the nebulizer (N), the light sheet (L), the camera (C) and 3D-traversing system (T). Right: reactor baseplate with bearings holding the first layer of spheres (black circles) and 312 holes for air distribution

content of the data-base by means of some characteristic example results of the PIV measurements. Access to the data and meta-data, that has been acquired in the frame of a Collaborative Research Centre (CRC/TR 287) of the German Research Foundation (DFG), can be given for interested readers through the authors.

2 Experimental Setup

The experimental set up for the measurement of gaseous flow fields inside a packed bed with PIV is shown in Fig. 1 left. A fixed bed reactor (R) holds a bcc-packing of spheres with a diameter $d = 40$ mm in up to 21 layers with 3×3 spheres in the first layer and every following odd layer. Odd layers are considered to be full layers, that touch the reactor walls, while even layers are weak layers due to the missing half spheres close to the reactor walls, leading to only 2×2 spheres in the even layers. Modules consisting of a weak and a full layer are built from individual polypropylene spheres. These modules can be stacked to generate the required bed height. The packing is placed in the reactor chamber with a cross sectional area of 0.32×0.32 m. The maximum bed height of 21 layers corresponds to approximately 0.5 m so that the reactor chamber with a height of 0.92 m provides an extended outlet zone to reduce the influence of the surroundings. The reactor is placed on a 3D-traversing unit (T) which allows movement to the respective measurement positions, without moving the optical measurements set-up.

Pressurised air controlled by a Bronkhorst Mass-Stream Controller (D-6371; 500 l/min air) is entering the reactor chamber with the packing material through the inlet zone (I) composed of a combination of a diffusor and honeycombs with additional small packing material (random arrangement of 4 mm glass spheres) to create homogeneous flow conditions. The final flow conditions for the flow entering the reactor chamber

are determined by a baseplate, see Fig. 1 right, which holds the sphere packing by nine bearings embedded into the plate. The spheres sit 0.8 mm deep in the bearings which define the bottom of the packing in the reactor chamber.

A hole pattern of 312 regularly arranged holes with a diameter of 4 mm allows the flow to pass in the centre part of the reactor while the regions close to the wall are omitted to reduce the wall channelling effect. The airflow is seeded with vaporized Di-Ethyl-Hexyl-Sebacat (DEHS) provided by a liquid nebulizer Type AGF 10.0 from Palas GmbH (N). By illuminating the measurement plane with a light sheet (L) crated by a light sheet optics and a Quantel Q-smart Twins 850 Nd:YAG PIV-laser with a maximum energy of 380 mJ/pulse and operated at 532nm, the scattered light from the tracer particles can be recorded by a camera (C) at 90° to the laser sheet. For the different measurement series, presented hereafter, different camera equipment and parameters were used as summarized in Table 1, to optimize the image quality in the respective setting.

A more detailed description of the experimental setup is provided by Velten et al. (2024).

For the synchronization of image acquisition and illumination, a PTU X from LaVision is used and controlled by the software Davis 8. This is also used for the evaluation of the particle fields by standard cross-correlation method (multi-pass, decreasing size from 64×64 to 32×32 pixels with 50%overlap.).

3 Inlet Conditions

The inlet conditions in the reactor are measured to characterize the flow field in the empty reactor. The aim is to proof that the reactor provides symmetric inlet conditions, as it is designed for, and to gain data which can be used as inlet conditions for numerical calculations. Therefore, different measurement positions and Re_P are considered as described in the following.

3.1 Volume Flow Rate and Particle Reynolds Number

The volume flow rate Q, defined with the cross sectional area of $A = 0.0175$ m^3 and the mean superficial velocity $v_{s,}$ can be controlled by the mass flow controller and is calculated based on the Re_P of interest.

$$Q = A \cdot v_s$$

The Re_P is based on the particle diameter $d_P = 40$ mm, the theoretical porosity $\varphi_{theo} = 0.32$ off the bcc-packing and the interstitial velocity v_{int} to ensure comparability for different systems by similarity approach, e.g. in terms of different sphere numbers and sizes.

$$v_{int} = \frac{v_s}{\varphi_{theo}}$$

$$Re_P = \frac{v_{int} \cdot \rho \cdot d_P}{\mu}$$

Table 1 Cameras, lenses and recording parameters for different measurement series

Measurement case	Camera	Lens	Aperture	Recording frequency (Hz)	Recorded images
Inlet flow (Sect. 3)	Imager LX 8M	Nikon Micro-Nikkor 60 mm f/2.8D	f5.6	1.67	100
Flow above the bed (Sec.t 4)	Imager LX 8M	Nikon AF Nikkor 35 mm f/2D	f5.6	2.5	100/300/1000
Flow inside the bed (Sect. 5)	Imager intense	Nikon Micro-Nikkor 105 mm f/2.8D	f5.6	2.5	300/1000

Table 2 Particle Reynolds numbers and the corresponding flow rates during the measurements

Re_P	[–]	200	300	400	500
Q	[l/min]	25.5	38.2	50.9	63.6

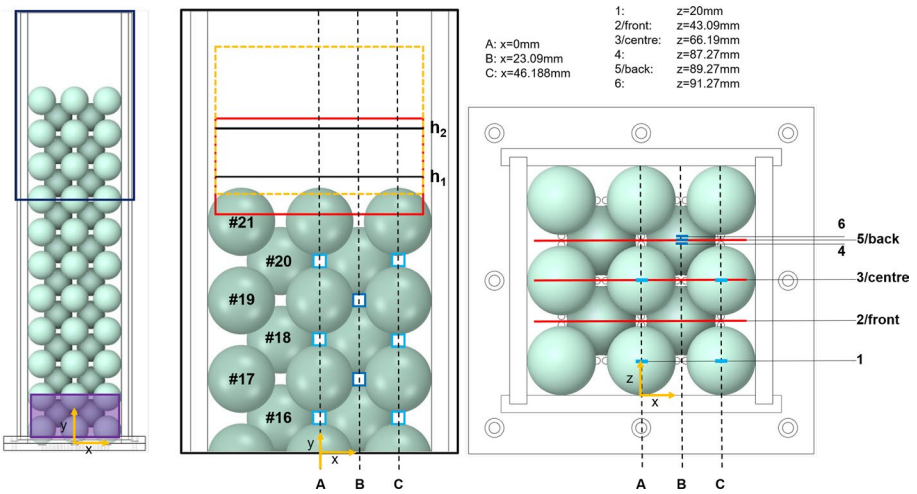

Fig. 2 Front view of the packed bed reactor with 21 layers of spheres in a bcc-packing (left). The purple rectangle marks the measurement zone for the inlet conditions (Sect. 3). The zoomed region (centre) into the layers of interest (16–21) is marked with a black rectangle. In this zoomed view, the regions where the flow fields were evaluated are marked with an orange dotted line for investigations of the bed height dependent flow pattern and with a red rectangle for the other measurements above the packed bed (Sect. 4). The small blue squares locate the flow data inside the packed bed (Sect. 5). Here, the dark blue marks the regions of interest for the full layers (17 and 19) and light blue represents the interstices in the even layers (16, 18 and 20). To clarify the positions, letters represent the position along the x-axis. The positions in the depth of the reactor (along the z-axis) are shown in the top view (right): While back/centre/front positions belong to the measurements above the ground plate in the empty reactor (inlet conditions, Sect. 3) and those above the bed, the numbers clarify the depth position in the interior of the packed bed. The combinations of letters and numbers are used to identify the flow regions for the data shown in Sects. 4 and 5

The material properties, density $\rho = 1.204\ \frac{\text{kg}}{\text{m}^3}$ and dynamic viscosity $\mu = 1.822 \cdot 10^{-5}\ \frac{\text{kg}}{\text{m·s}}$, are selected for ambient temperature and pressure ($T = 20$ °C and $p = 1$ bar).

Measurements are carried out in a range of $Re_P = 200$ to 500. An overview of Re_P and the corresponding volume flow rates during the measurements is given in Table 2.

3.2 Measurement Position and Coordinate System

The inlet flow is measured above the ground plate as illustrated in Fig. 2 left showing the front view of the packed bed reactor by a purple rectangle. Note that for the measurements of the inlet conditions no packing was placed in the reactor. Since the symmetric inlet flow conditions should be validated by these measurements in the empty reactor above the ground plate, different measurement positions, one in the centre of the reactor, the second

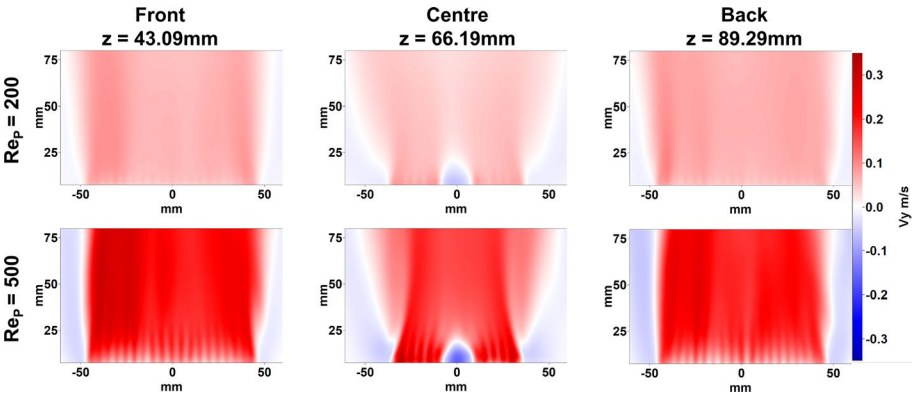

Fig. 3 Averaged fields of the main vertical flow component v_y for the inlet flow in the empty reactor measured above the ground plate for three different measurement positions (front, centre, back), for the minimum and maximum measured $Re_P = 200$ and 500

in the front between the later position of the first and second sphere and a third in the back between the later position of the second and third sphere, have been chosen (Fig. 2 right, positions 3, 2 and 5 respectively, marked with red lines). Assuming that we are able to proof symmetrical conditions, the coordinate system is defined in the following way (Fig. 2): the origin of the horizontal axis (x-axis) is the centre of the reactor, while the vertical axis (y-axis) starts on top of the base plate. For the depth (z-axis), the inner side of the front wall, where the first spheres touch the wall, is chosen as origin.

In Fig. 2, also the other measurement positions used in this work are identified. They will be described in detail in the corresponding sections.

3.3 Results and Symmetry

Figure 3 shows the averaged fields of the vertical flow velocity v_y for the aforementioned three measurement positions above the ground plate in the empty reactor. $Re_P = 200$ and 500 where chosen to represent the flow conditions at minimum and maximum velocity. The vertical flow component v_y is considered as the main flow component because of the direction of the flow in the empty reactor. The averaged value of the horizontal velocity component v_x is around two to three magnitudes lower than that for the vertical velocity v_y.

The flow structure appearing in the empty reactor for both Re_P is similar to each other while varying in magnitude. While the main flow goes straight to the reactor outlet, recirculation zones can be found in the regions close to the reactor walls as well as for the centre position in the horizontal centre (around $x = 0$ mm) directly above the ground plate. Both flow structures can be explained by the geometry. In the rim region of the reactor the hole pattern on the baseplate is omitted, blocking the flow in that region and leading to the recirculation zones near the walls. For the centre position, the smaller recirculation zone directly above the ground plate appears due to a bearing embedded in the ground plate, where later on the central sphere is placed.

Based on this data, difference images are calculated (Fig. 4) with two different objectives: first, to verify if the flow for each measurement position (front, centre and back) is symmetrical. Therefore, the left image half is subtracted from the right

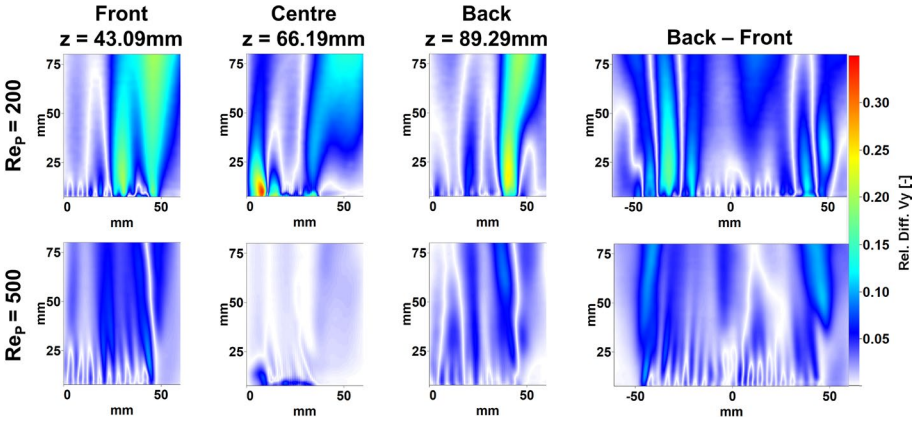

Fig. 4 Relative differences (0 … 1) of the main vertical flow component v_y normalized by the maximum velocity value for front, centre and back position, based on the averaged fields and the difference between back and front position for $Re_P = 200$ and 500

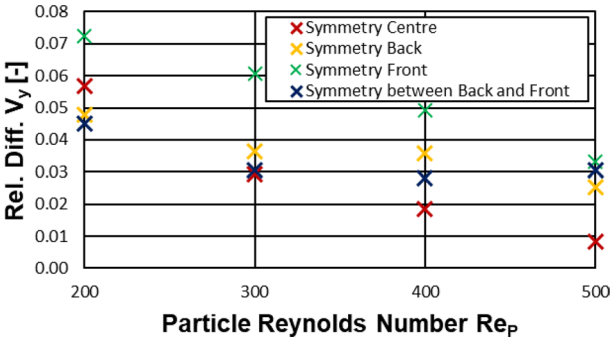

Fig. 5 Averaged relative differences based on averaged fields of the main vertical flow component v_y for Re_P in the range of 200–500

one and normalized by the maximum vertical velocity value. Second, the difference between front position and back position, normalized by the maximum value of the back position, allows to verify the symmetry along the z-axis.

Comparing the difference images for the two different Re_P it is obvious that higher deviations from ideal symmetric conditions (given by a relative difference of 0.0) exist for the smaller $Re_P = 200$. Stronger deviations can be found in regions where high velocity gradients exist. This is the case for the strong vertical flow and the recirculation zones where locally high difference values can appear up to 0.3 for $Re_P = 200$.

For a summery and better comparability of all measured Re_P, Fig. 5 provides the averaged values from the relative difference images for Re_P in the range of 200–500. While getting lower relative differences for higher Re_P, the differences are highest for the front measurement position, but not exceeding 0.08, that means 8% of the maximum velocity.

If we consider the influence of the surrounding atmosphere and also manufacturing tolerances, the system can nevertheless be regarded as symmetrical. Now, by assuming a symmetric geometry of the reactor, the packing and the inlet flow, also symmetric flow conditions inside and above the packed bed can be expected.

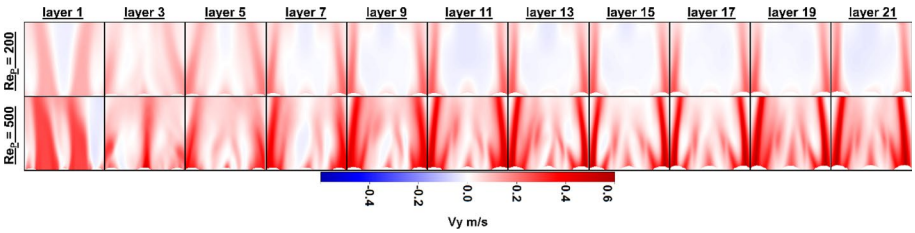

Fig. 6 Averaged fields of the vertical velocity component v_y above every odd layer (1–21) for the minimum and maximum $Re_P = 200$ and 500

4 Flow Above the Bed

4.1 Bed Height Independent Flow

The sphere modules allow for measurements above every odd layer of spheres, which correspond to the full layers. To choose the full height of the packing, from which the surface flow field becomes independent from the number of superimposed sphere layers, flow fields were evaluated for the minimum and maximum $Re_P = 200$ and 500 at the surface of the bed in the back position according to Fig. 2 (orange dashed rectangle).

The findings are illustrated in Fig. 6 as averaged fields of the vertical velocity component v_y. It can be seen that for lower layers the flow varies strongly. Starting from layer 11 the aspect of the flow field becomes similar to the layers above. Only a small change in the upper part of the shown field of view is still visible. This might be due to influences from the surrounding atmosphere.

Based on this data, the maximum bed height for the packing was chosen with 21 layers, to ensure only weak influences of the surroundings and allowing for height independent measurements in layers 16–21. All layers below (1–16) have then be connected to each other, to avoid reassembling of the packing in the following measurements and provide a better reproducibility.

To ensure that the flow field was not changed significantly by the connection of the modules, that introduces small bridges between the glued spheres, the measurements where repeated in layer 17, 19 and 21 during longer time periods off 120 s for $Re_P = 200$ and 400 s for $Re_P = 500$. The region of interest was reduced to approximately one sphere diameter ($d_P = 40$ mm) above the top layer of the bed, as shown in Fig. 2 (red coloured rectangle) to reduce the influence of the surroundings.

Two different heights above the top layer of spheres ($h_1 = 11$ mm and $h_2 = 39$ mm; also shown as black lines in Fig. 2) were chosen for the comparison and the results for the three different layers (17, 19 and 21) are plotted in Fig. 7. On the left side, the plots for the averaged vertical velocity component v_y and on the right side the averaged horizontal velocity components v_x are shown for $Re_P = 200$ (blue) and $Re_P = 500$ (red). The overall aspect of the curves is the same for the different bed heights (different symbols) and only small deviations in terms of the position and the magnitude of the maximum and minimum peak velocities appear, especially for the higher $Re_P = 500$. For the latter, the flow is not that stable compared to $Re_P = 200$ and fluctuations lead to the aforementioned differences. A detailed discussion of the flow structures including the fluctuations will be given in Sect. 4.2. Comparing the profiles for the two different distances from the top of the bed, it

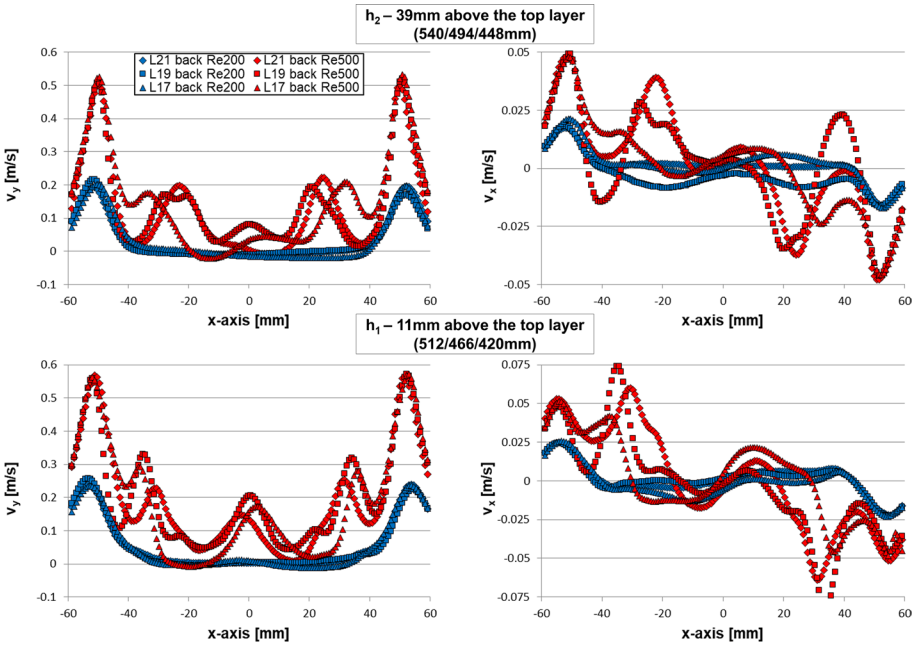

Fig. 7 Profiles of the averaged vertical velocity component v_y (left) and the averaged horizontal velocity component v_x (right) for two different heights ($h_1 = 11$ mm (bottom) and $h_2 = 39$ mm (top)) above the bed for 17, 19 and 21 layers with $Re_P = 200$ and 500

becomes clear, that with an increasing distance to the top layer the influence of the ambient is more pronounced.

Nevertheless, it can be concluded that with a maximum bed height of 21 layers of spheres, the flow can be considered as independent from the bed height so that further discussions of the flow structures above the bed will only be carried out for the 21-layer case.

4.2 Flow Structure Above the Bed (21 layers)

The flow above 21 layers of the packing should be symmetrical due to the symmetric inlet conditions (Sect. 3.3) and symmetric packing geometry. The front and the back position (position between the first to second sphere and the second to third sphere seen from the camera respectively) should therefore show identical flow fields. In Fig. 8 the averaged vertical and horizontal velocity components for $Re_P = 200$ and 500 are shown for both positions. The flow itself is characterised by two vertical jets in the near wall region where the highest velocities appear. This behaviour is expected due to the missing half spheres close to the reactor walls in the even layers, leading to a locally higher porosity and a reduced flow resistance and is reported by many authors in different packed bed configurations (e.g. (Patil and Liburdy 2013; Nguyen et al. 2019)). In the centre of the reactor a region with low velocities close to 0 m/s, appears as a stable recirculation zone for lower Re_P. For $Re_P = 500$ the flow field is more complicated with an upwards oriented

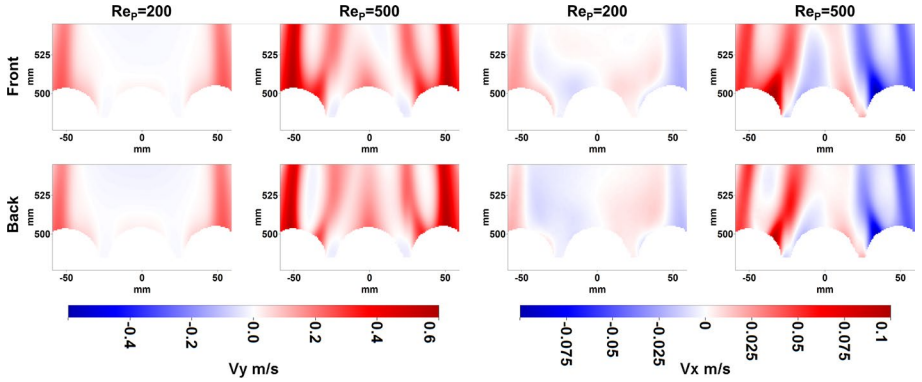

Fig. 8 Averaged vertical (left) and horizontal (right) velocity fields for $Re_P = 200$ and 500 for front (top) and back (bottom) position

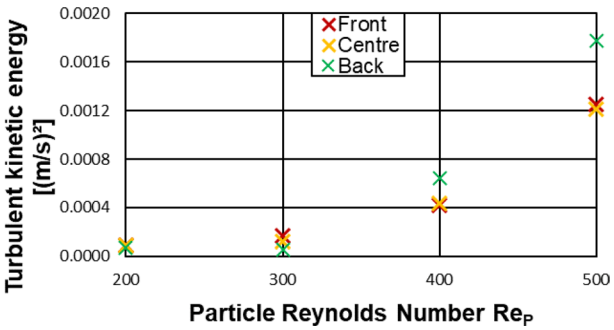

Fig. 9 Turbulent kinetic energy TKE for the front, centre and back positions in the range from $Re_P = 200$ to 500

region in the centre and two recirculation zones on both sides, where the velocity is close to 0 m/s.

While for $Re_P = 200$ the flow fields of back and front position are almost identical for both velocity components, differences are more obvious for $Re_P = 500$. The flow is more unstable for higher Re_P which can be shown by evaluating the turbulent kinetic energy (TKE) given by the following equation for the two dimensional case including the horizontal velocity v_x with $i = 1$ and the vertical velocity v_y with $i = 2$ and its averaged values $\overline{v}_i$ (LaVision GmbH Jul-2019).

$$TKE = \sum_{i=1}^{2} \frac{3}{4} \left(v_i - \overline{v}_i \right)^2$$

Figure 9 summarizes the TKE calculated from 300 ($Re_P = 200$ and 300) or 1000 ($Re_P = 400$ and 500) images of each case for the different measurement positions and all Re_P. While the flow for lower Re_P can be considered as stable with low TKE values, the TKE for the higher Re_P increases. Up to $Re_P = 400$ the flow structure does not change significantly during the measurements while for $Re_P = 500$ different structures appear and the TKE increases significantly.

These different structures are not much apparent in the averaged velocity fields as shown up to now. Therefore, Fig. 10 shows the fluctuating flow structures based on selected

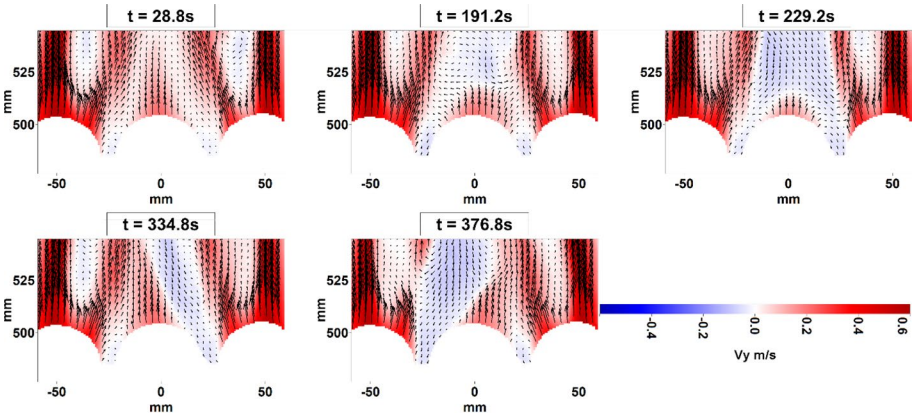

Fig. 10 Fluctuating flow structures based on the vertical velocity v_y of snap shot images for $Re_P = 500$ (back position) at different times with the vector field as an overlay

snapshot images at $Re_P = 500$ for the back position. In the background, the vertical velocity component, which is considerably higher than the horizontal component, is plotted in false colour. The vector field is added as an overlay to highlight the different flow structures. The upper row shows three different symmetric instants, which appeared during the measurement series: the first ($t = 28.8$ s) is similar to the averaged velocity field as shown before in Fig. 8; the second ($t = 191.2$ s) and the third ($t = 229.2$ s) are showing symmetrical flows, but with a more pronounced recirculation zone in the centre, where a vortex pair appears. This vortex pair is much bigger in the third image. In-between these structures, the recirculation zone is attaching and detaching as illustrated exemplarily in the two images of the lower row ($t = 334.8$ and 376.8 s). This detachment does not follow any obvious pattern or frequency (at least detectable with the acquisition frequency around 2 Hz used here, see Table 1) and explains why even for often repeated measurements asymmetric averaged fields are obtained. Besides the influence of the ambient and manufacturing uncertainties, this explains the stronger deviations at higher Re_P (Fig. 6) as well as the afore discussed slight dissymmetry between back and front position (Fig. 8). In the following, only the centre and back positions will be analysed further.

The velocity profiles for the vertical and horizontal velocity component at two different heights ($h_1 = 11$ mm and $h_2 = 39$ mm) above the bed are shown in Fig. 11. For all Re_P the jets on both sides of the reactor can be seen in the profiles for both velocity components. This indicates that the general flow structure is not influenced by the increasing Re_P as already reported by Patil and Liburdy (2013) for low Reynolds numbers. It has to be taken into account that the horizontal velocity is about one order of magnitude smaller than the vertical on, so that the following discussion is focused on the vertical velocity plots (left). The magnitude of the jets is increasing with increasing Re_P, but they are always located around $x \approx \pm 50$ mm. Starting from $Re_P = 300$, additional local maxima appear in the profiles. In the centre of the reactor ($x = 0$ mm), a cavity exists, where the flow is not blocked by underlying sphere layers in the back position. Here, a local vertical velocity maximum shows up and grows with Re_P and when approaching the bed surface (lower profiles in Fig. 11, h_1, compared to the upper profiles, h_2), but with much lower magnitudes compared to the jets in the near wall region. From $Re_P = 400$ additional jets appear arround $x \approx \pm 30$ *mm* and are shifted closer to the centre ($x \approx \pm 22$ *mm*) for $Re_P = 500$.

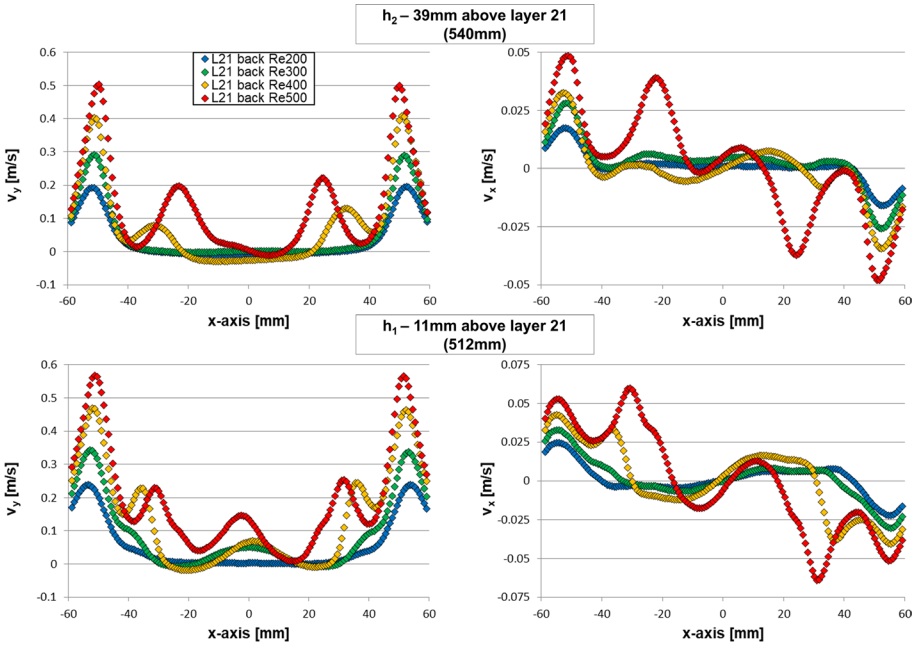

Fig. 11 Profiles of the vertical flow component v_y (left) and the horizontal flow component v_x (right) for two different heights ($h_1 = 11$ mm (lower) and $h_2 = 39$ mm (upper)) of the back position above 21 layers for $Re_P = 200 - 500$

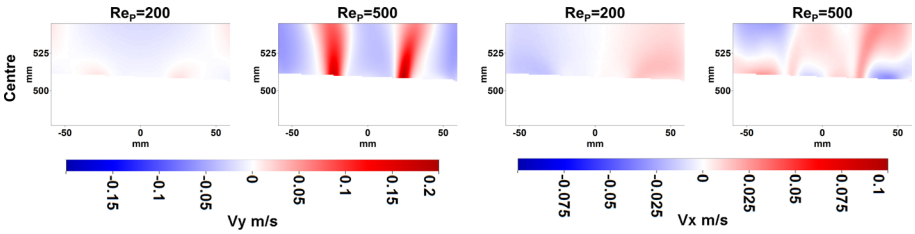

Fig. 12 Averaged vertical and horizontal velocity fields for $Re_P = 200$ and 500 at the centre position

These positions correspond to the void space between the sphere rows, that induce these additional vertical flows with increasing velocity fluctuations at higher Reynolds number. This suggest that the flow velocity is following the prorosity of the bed as stated by Giese et al (1998).

The flow field at the centre position on the top of the centre sphere shows a completely different aspect (Fig. 12). The flow passes besides the centred sphere resulting in two jets at $x \approx \pm 25$ mm. In comparison with the back position, the two outer spheres, having contact points to the wall, disable the flow to pass. In this position the laser light sheet is blocked by the right sphere, creating a shadow which does not allow to gain measurement signals below. For the centre position the magnitudes of the vertical and horizontal velocity components are more similar, but much lower than for the back position in terms of the vertical component. As shown in the profiles of Fig. 13, the vertical velocity peaks are

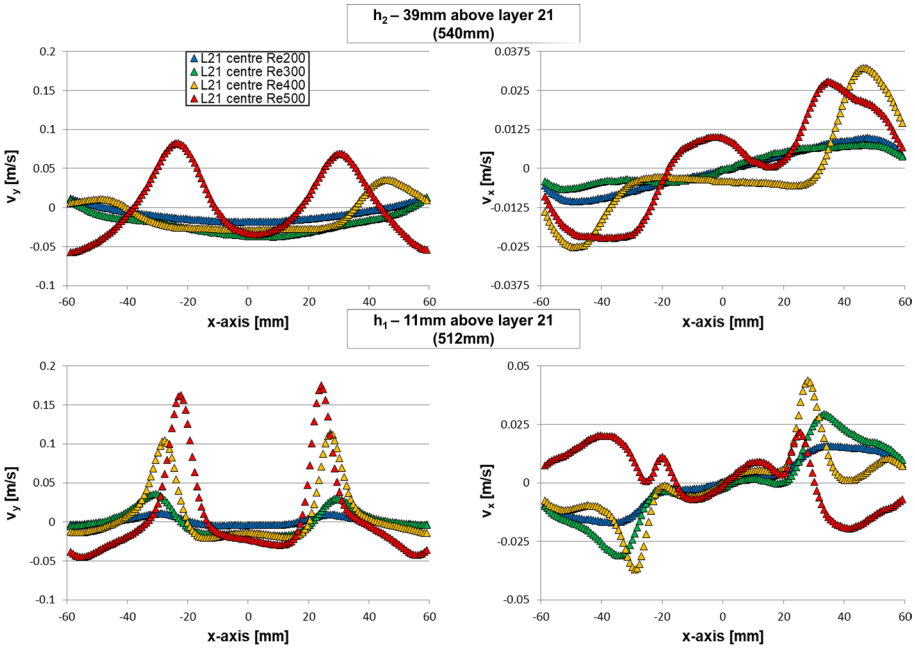

Fig. 13 Profiles of the vertical velocity component v_y (left) and the horizontal velocity component v_x (right) for two different heights ($h_1 = 11$ mm (lower) and $h_2 = 39$ mm (upper)) of the centre position for $Re_P = 200$ –500

decreasing with the height above the bed, and the jets do not even exist anymore for lower Re_P (see Fig. 13, position h_2). The symmetry of the flow along the x-axis is also obvious from these profiles, apart from the horizontal velocity for $Re_P = 500$ at h_1. Following Fig. 9, at $Re_P = 500$ the *TKE* is the highest and these fluctuations can lead to an asymmetric averaged flow field. Also, when analysing visually the complete time series of the measurements, low frequency oscillations of the flow can be observed, as shown in Fig. 10 for the back position.

Due to the general characteristics of the flow above the bed, symmetry and similar flow structures for the investigated Re_P *range*, it can be assumed, that also inside the packed bed symmetric structures and similar flow fields for the different Reynolds numbers will exist, which will be discussed in the following Sect. 5.

5 Flow Inside the Packed Bed

Inside the bed (layer 16–20), the field of view is drastically reduced for standard PIV techniques and limited to a small region in the cavities which are easily accessible without disturbing the laser light sheet and allowing direct optical access for the camera view. Due to the symmetry of the flow, only the right half of the packing is considered as shown in Fig. 2 with the blue rectangles and lines.

The resulting mean velocity magnitudes for a bed with a total height of 21 layers are shown in Figs. 14 and 15 with the vector field as an overlay to illustrate the flow structure

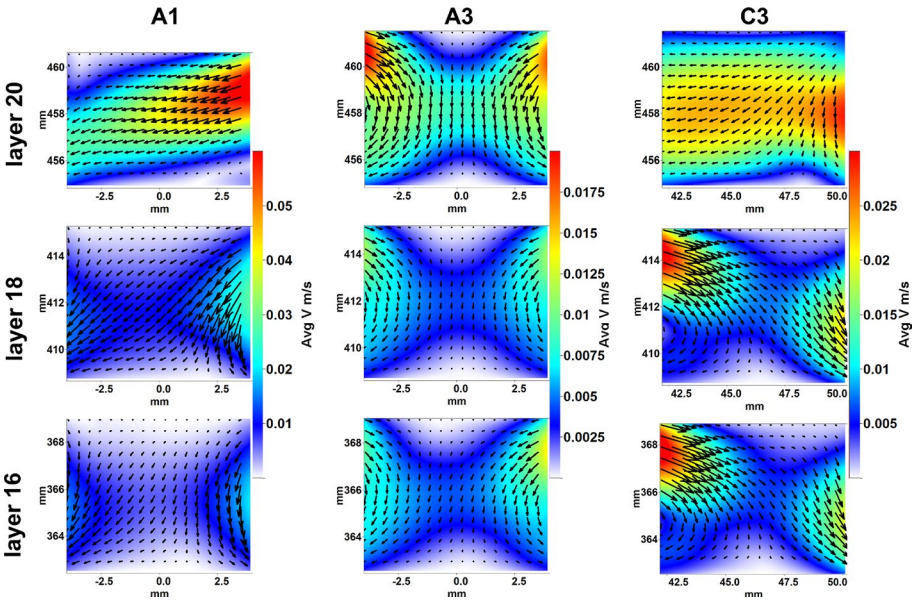

Fig. 14 Velocity magnitude of the flow in different interstices inside even layers (16, 18 and 20) of the packed bed (total height of 21 layers) with the vector fields as an overlay for $Re_P = 500$ (mind the different colour and vector scales)

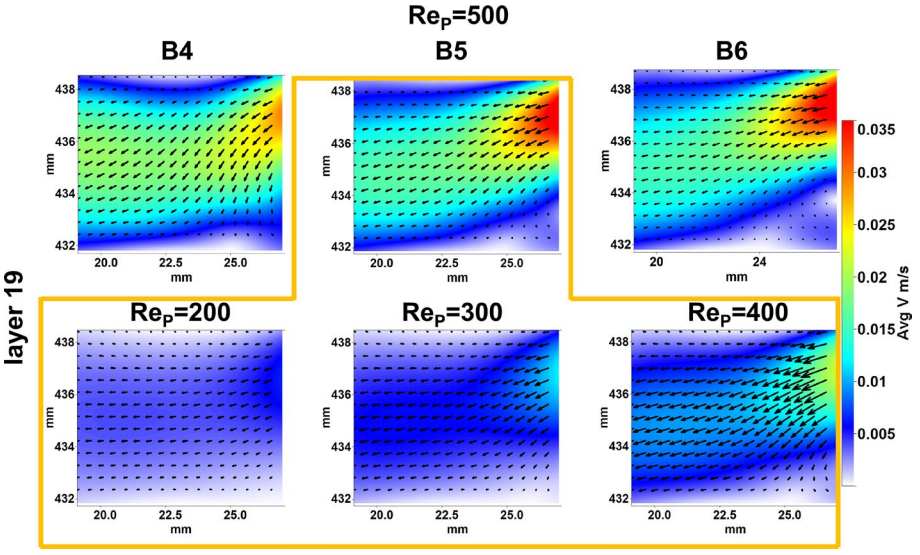

Fig. 15 Velocity magnitude of the flow in different measurement planes (B4/B5/B6) inside layer 19 of the packed bed with the vector fields as an overlay for $Re_P = 500$ (top row) and for position B5 and different Re_P (bottom row)

and direction for $Re_P = 500$. Only every fourth vector is shown and the scaling of the vectors varies from one image to the other for better visibility of the low velocity cases.

In Fig. 14, the results of the even layers (16, 18 and 20) are presented. While position "A" is the centre of the horizontal axis ($x = 0$ mm), the "C" position corresponds to $x = 46.19$ mm and describes the pore close to the wall. The number characterises the position in the depth, where "1" represents the measurement plane at $z = 20$ mm on top of the first row of underlying spheres, and "3", at $z = 66.19$ mm is the same plane as the centre position from Sects. 3 and 4, that means on top of the centre row of spheres.

It can be observed that the flow fields further from the packing surface (layer 16 and 18) show rather similar flow fields for each individual position with only slight variations in the velocity magnitude. On the other hand, the flow fields in the 20th layer, near the surface of the bed, show a different behaviour with higher velocity magnitude and different structures. For "A1" and "C3", the flow field changes completely leading even to another orientation of the flow. For "A1" the vortex pair, which exists deeper inside the bed, disappears and a stronger horizontal flow is apparent. For "C3", the horizontal flow direction is reversed compared to layer 16 and 18. The flow field of "A3" only shows a change in velocity magnitude. This position is the position with the lowest velocities (mind the colour scales in Fig. 14) compared to the other measurement zones and situated in the centre of the reactor while "A1" and "C3" are closer to the jets passing through the region with higher porosity close to the walls and leading to generally higher velocities. Due to the higher resistance caused by the lower porosity in the centre of the packing, lower velocities appear and also might explain the remaining flow structure. The different behaviour of the flow in layer 20 can be explained by its location in the bed. Layer 20 is the layer directly under the top where the flow gets released to the free surface, which influences on the flow structure inside the bed. This corresponds also to the outlet region which is mentioned by Giese et al. (1998) where different flow profiles in comparison to the constant profiles deeper in the packed bed were observed.

The effect of almost constant flow fields for different cavity height in the bed is noticeable for the interstices in the odd layers (17, 19), where, due to symmetry, measurements have been executed only in the "B" position ($x = 23.09$ mm, cavity between the centre and right sphere, between the second and third row in the depth). Here, three different planes in the depth of the cavity have been examined: "5", in the centre of the cavity, corresponds to the back position of Sect. 3 ($z = 89.27$ mm), "4" ($z = 87.27$ mm) is shifted 2 mm to the front and "6" ($z = 91.27$ mm) 2 mm to the back, in order to cover almost the entire depth between two sphere rows. No significant change of the flow structure inside such an interstice exists, as shown in the upper row of Fig. 15, for layer 19 of the bed. Only for "B4", the front plane of the cavity, a slightly lower magnitude was found, that might be attributed to the approach of the ahead lying sphere.

The influence of Re_P inside the packing is shown in the lower part of Fig. 15 for the "B5" position (orange frame). At different Re_P similar flow structures exist, with only varying magnitude as it was also the case for the flow above the bed.

The flow inside the packing is very stable compared to the surface flow as can be seen by comparing Figs. 9 and 16. The latter shows two diagrams of the averaged *TKE* values for two different measurement positions inside the packed bed ("A3" left and "C1" right) for the even layers (16, 18 and 20) and all Re_P. These positions where chosen to illustrate the trend of the *TKE* also for all other measurement positions. In general, the *TKE* of the flow inside the packing is one to four magnitudes lower than above the packing for $Re_P = 200$, which already was considered as stable. It increases with Re_P also for the flow inside the bed. Although for the lower $Re_P = 200$ and $Re_P = 300$ no strong dependence of the height

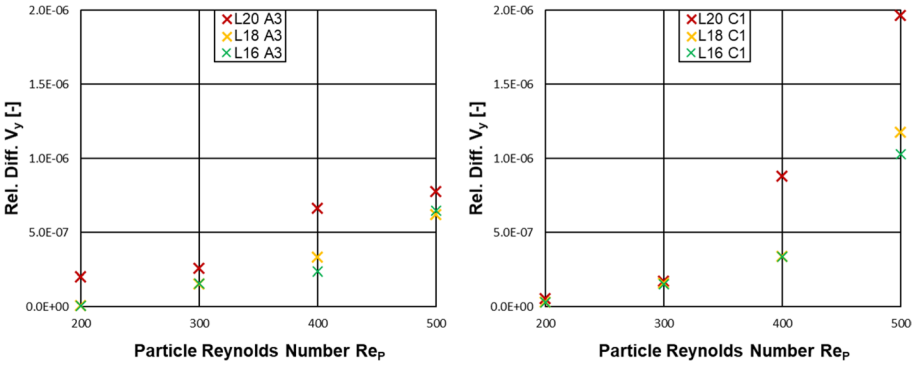

Fig. 16 TKE for "A3" (left) and "C1"(right) positions in the even layers (16, 18 and 20) in the range from $Re_P = 200$ to 500

position in the packing can be observed, for higher $Re_P = 400$ and $Re_P = 500$ it is found that the *TKE* increases when approaching the surface of the bed (layer 20). This confirms the findings from Giese et al. (1998) and Hassan and Dominguez-Ontiveros (2008), where increasing fluctuations and vorticity was determined with decreasing distance from the bed surface.

Comparing different positions in the packing for a fixed height, for example "A3" and "C1" as given in Fig. 16, the *TKE* is not constant. At "A3", in the reactor centre, where the lowest velocities were measured (see Fig. 14) also lower *TKE* is determined. The "C1" position, which is close to the reactor walls where the strong wall jets go through the bed, also the TKE is higher, while still remaining at a very low level compared to the surface flow.

6 Conclusions

In this work, extensive measurements of gas flow fields inside a model packed bed have been executed by PIV. This data-base serves as validation data for CFD and DEM calculations of packed bed reactors (Gorges et al. 2024; Neeraj et al. 2023) and is accessible to interested readers through the authors. Here, the results are presented exemplarily and the flow fields are discussed in terms of inlet conditions to the empty reactor, symmetry and height independent flow structure above the bed as well as measurements inside the bed for Re_P in a range from 200 to 500. The inlet conditions were found to be reasonably symmetric, as it was initially intended by a symmetric construction of the bed and reactor. As well, the flow above the bed becomes symmetric and suffers only from ambient influences and probably slight, unavoidable production inaccuracies. The influence of the free surface to the highest packing layers becomes evident through the measurements in the interstices of the bed. While the flow structures in the lower layers are repeated, they are rather different in the highest interstices, just under the free surface of the bed. In the range of the study, the Reynolds number does not fundamentally change the structure of the flow fields. Only the velocity magnitude is increasing with increasing Reynolds number.

Since the part of the bed, accessible for optical measurement techniques, is rather small compared to the total fluid volume, measurements behind transparent spheres are currently

carried out, that will be post-processed by a ray tracing method. This will allow to correct for the optical distortions, induced by the spheres to the PIV particle fields. Thus velocity fields will also be accessible in regions behind spheres and a complete flow field inside the packed bed will be obtained. First preliminary results of this ongoing work can be found in (Ebert et al. 2022; Velten et al. 2022).

Acknowledgements Funded by the Deutsche Forschungsgemeinschaft (DFG, German Research Foundation)—Project-ID 422037413—TRR 287. Péter Kováts and our students Zahin Thamed, Clemens Knoche and Aritra Rayan are acknowledged for their help during experiments.

Authors' Contributions All authors contributed to the study conception and design. Material preparation, data collection and analysis were performed by Christin Velten and Katharina Zähringer. The first draft of the manuscript was written by Christin Velten and all authors commented on previous versions of the manuscript. All authors read and approved the final manuscript.

Funding Open Access funding enabled and organized by Projekt DEAL. Funded by the Deutsche Forschungsgemeinschaft (DFG, German Research Foundation)—Project-ID 422037413—TRR 287.

Data Availability For access to the used datasets please contact the corresponding author (christin.velten@ovgu.de).

Declarations

Conflict of interest Both authors declare that they have no conflict of interest.

Ethical Approval Not applicable.

References

Ebert, M., Velten, C., Zähringer, K., Lessig, C., Vad, J.: Efficient PIV measurements in the interior of complex, transparent geometries. In: Conference on Modelling Fluid Flow (CMFF'22) (August 30 - September 2, 2022 Budapest/Hungary), 78–86 (2022)

Giese, M., Rottschafer, K., Vortmeyer, D.: Measured and modeled superficial flow profiles in packed beds with liquid flow. AIChE J. **44**(2), 484 (1998)

Gladden, L.F., Akpa, B.S., Anadon, L.D., Heras, J.J., Holland, D.J., Mantle, M.D., Matthews, S., Mueller, C., Sains, M.C., Sederman, A.J.: Dynamic MR imaging of single- and two-phase flows. Chem. Eng. Res. Des. **84**(4), 272–281 (2006)

Gorges, C., Brömmer, M., Velten, C., Wirtz, S., Mahiques, E.I., Scherer, V., Zähringer, K., van Wachem, B.: Comparing two IBM implementations for the simulation of uniform packed beds. Particuology **86**, 1–12 (2024)

Harshani, H.M.D., Galindo-Torres, S.A., Scheuermann, A., Muhlhaus, H.B.: Experimental study of porous media flow using hydro-gel beads and LED based PIV Meas. Sci. Technol. **28**(1), 15902 (2017)

Hassan, Y.A., Dominguez-Ontiveros, E.E.: Flow visualization in a pebble bed reactor experiment using PIV and refractive index matching techniques. Nucl. Eng. Des. **238**(11), 3080–3085 (2008)

Huang, A.Y.L., Huang, M.Y.F., Capart, H., Chen, R.-H.: Optical measurements of pore geometry and fluid velocity in a bed of irregularly packed spheres. Exp. Fluids **45**(2), 309–321 (2008)

Khayamyan, S., Lundström, T.S., Gren, P., Lycksam, H., Hellström, J.G.I.: Transitional and turbulent flow in a bed of spheres as measured with stereoscopic particle image velocimetry. Transp. Porous Med. **117**(1), 45–67 (2017a)

Khayamyan, S., Lundström, T.S., Hellström, J.G.I., Gren, P., Lycksam, H.: Measurements of transitional and turbulent flow in a randomly packed bed of spheres with particle image velocimetry. Transp Porous Med **116**(1), 413–431 (2017b)

Kováts, P., Thévenin, D., Zähringer, K.: Experimental investigation of flow fields within cavities of coarse packed bed Fachtagung "Lasermethoden in der Strömungsmesstechnik", 54-1-7 (2015)

Larsson, I.A.S., Lundström, T.S., Lycksam, H.: Tomographic PIV of flow through ordered thin porous media. Exp. Fluids **59**(6), 1–7 (2018)

LaVision GmbH: 8.4 DaVis software manual, (2019). https://www.lavision.de/de/download.php?id=3020

Lovreglio, P., Das, S., Buist, K.A., Peters, E.A.J.F., Pel, L., Kuipers, J.A.M.: Experimental and numerical investigation of structure and hydrodynamics in packed beds of spherical particles. AIChE J. **64**(5), 1896–1907 (2018)

Martins, F., Da Carvalho Silva, C., Lessig, C., Zähringer, K.: Ray-Tracing based image correction of optical distortion for PIV measurements in packed beds. J. Adv. Opt. Photonics **1**(2), 71–94 (2018a)

Martins, F., Da Carvallo Silva, C., Lessig, C., Zähringe, K.: Ray-tracing based image correction of optical distortions caused by transparent spheres for application in PIV. In: 19th International Symposium on the Application of laser and Imaging Techniques to Fluid Mechanics (16–19 July, 2018b Lisbon), pp. 2.8.2 (2018b)

Morales, M., Spinn, C.W., Smith, J.M.: Velocities and effective thermal conductivities in packed beds. Ind. Eng. Chem. **43**(1), 225–232 (1951)

Moroni, M., Cushman, J.H.: Statistical mechanics with three-dimensional particle tracking velocimetry experiments in the study of anomalous dispersion. II. Experiments. Phys. Fluids **13**(1), 81–91 (2001)

Neeraj, T., Velten, C., Janiga, G., Zähringer, K., Namdar, R., Varnik, F., Thévenin, D., Hosseini, S.A.: Modeling gas flows in packed beds with the lattice Boltzmann method: validation against experiments Flow. Turbul. Combust. **111**(2), 463–491 (2023)

Nguyen, T., Muyshondt, R., Hassan, Y.A., Anand, N.K.: Experimental investigation of cross flow mixing in a randomly packed bed and streamwise vortex characteristics using particle image velocimetry and proper orthogonal decomposition analysis. Phys. Fluids **31**(2), 25101 (2019)

Patil, V.A., Liburdy, J.A.: Flow characterization using PIV measurements in a low aspect ratio randomly packed porous bed. Exp. Fluids **54**(4), 1–19 (2013)

Poelma, C.: Measurement in opaque flows: a review of measurement techniques for dispersed multiphase flows. Acta Mech. **231**(6), 2089–2111 (2020)

Pokrajac, D., Manes, C.: Velocity measurements of a free-surface turbulent flow penetrating a porous medium composed of uniform-size spheres. Transp. Porous Med. **78**(3), 367–383 (2009)

Schwartz, C.E., Smith, J.M.: Flow distribution in packed beds. Ind. Eng. Chem. **45**(6), 1209–1218 (1953)

Sederman, A.J., Johns, M.L., Bramley, A.S., Alexander, P., Gladden, L.F.: Magnetic resonance imaging of liquid flow and pore structure within packed beds. Chem. Eng. Sci. **52**(14), 2239–2250 (1997)

Shaffer, F., Gopalan, B., Breault, R.W., Cocco, R., Karri, S.R., Hays, R., Knowlton, T.: High speed imaging of particle flow fields in CFB risers. Powder Technol. **242**, 86–99 (2013)

Suekane, T., Yokouchi, Y., Hirai, S.: Inertial flow structures in a simple-packed bed of spheres. AIChE J. **49**(1), 10–17 (2003)

Velten, C., Ebert, M., Lessig, C., Zähriger, K.: Ray tracing based reconstruction of PIV measurements in the outlet zone of gaseous flow in packed beds Lisbon. In: 20th International Symposium on the Application of Laser and Imaging Techniques to Fluid Mechanics (11–14 July, 2022, Lisbon), 51/1–11 (2022)

Velten, C., Ebert, M., Lessig, C., Zähringer, K.: Ray tracing particle image velocimetry–Challenges in the application to a packed bed. Particuology **84**, 194–208 (2024)

Wiederseiner, S., Andreini, N., Epely-Chauvin, G., Ancey, C.: Refractive-index and density matching in concentrated particle suspensions: a review. Exp. Fluids **50**(5), 1183–1206 (2011)

Wood, B.D., Apte, S.V., Liburdy, J.A., Ziazi, R.M., He, X., Finn, J.R., Patil, V.A.: A comparison of measured and modeled velocity fields for a laminar flow in a porous medium. Adv. Water Resour. **85**, 45–63 (2015)